



Published in final edited form as:

Med Phys. 2008 February ; 35(2): 446–455.

Comparison of diffuse optical tomography of human breast with whole-body and breast-only positron emission tomography

Soren D. Konecky^{a)},

Department of Physics and Astronomy, University of Pennsylvania, 209 South 33rd Street, Philadelphia, Pennsylvania 19104

Regine Choe,

Department of Physics and Astronomy, University of Pennsylvania, 209 South 33rd Street, Philadelphia, Pennsylvania 19104

Alper Corlu,

Department of Physics and Astronomy, University of Pennsylvania, 209 South 33rd Street, Philadelphia, Pennsylvania 19104

Kijoon Lee,

Department of Physics and Astronomy, University of Pennsylvania, 209 South 33rd Street, Philadelphia, Pennsylvania 19104

Rony Wiener,

Department of Radiology, University of Pennsylvania, 110 Donner, 3400 Spruce St., Philadelphia, Pennsylvania 19104

Shyam M. Srinivas,

Department of Radiology, University of Pennsylvania, 110 Donner, 3400 Spruce St., Philadelphia, Pennsylvania 19104

Janet R. Saffer,

Department of Radiology, University of Pennsylvania, 110 Donner, 3400 Spruce St., Philadelphia, Pennsylvania 19104

Richard Freifelder,

Department of Radiology, University of Pennsylvania, 110 Donner, 3400 Spruce St., Philadelphia, Pennsylvania 19104

Joel S. Karp,

Department of Radiology, University of Pennsylvania, 110 Donner, 3400 Spruce St., Philadelphia, Pennsylvania 19104

Nassim Hajjioui,

Department of Imaging and Visualization, Siemens Corporate Research, 755 College Road East, Princeton, New Jersey 08540

Fred Azar, and

Department of Imaging and Visualization, Siemens Corporate Research, 755 College Road East, Princeton, New Jersey 08540

Arjun G. Yodh

Department of Physics and Astronomy, University of Pennsylvania, 209 South 33rd Street, Philadelphia, Pennsylvania 19104

a)Author to whom correspondence should be addressed. Electronic mail: skonecky@physics.upenn.edu.

Abstract

We acquire and compare three-dimensional tomographic breast images of three females with suspicious masses using diffuse optical tomography (DOT) and positron emission tomography (PET). Co-registration of DOT and PET images was facilitated by a mutual information maximization algorithm. We also compared DOT and whole-body PET images of 14 patients with breast abnormalities. Positive correlations were found between total hemoglobin concentration and tissue scattering measured by DOT, and fluorodeoxyglucose (^{18}F -FDG) uptake. In light of these observations, we suggest potential benefits of combining both PET and DOT for characterization of breast lesions.

Keywords

diffuse optical tomography; positron emission tomography; breast cancer; near-infrared imaging; breast imaging; tumor metabolism; ^{18}F fluorodeoxyglucose; hypoxia

I. Introduction

Breast cancer characterization and diagnosis is an active sub-field of diffuse optics research.^{1–8} Diffuse optical tomography (DOT), in particular, offers the possibility for noninvasive imaging of functional information about tumor physiology.⁹ Recently, experimenters have begun to compare and incorporate traditional medical diagnostics such as magnetic resonance imaging (MRI),^{10–12} ultrasound,¹³ and x-ray mammography¹⁴ with the optical measurement. A typical approach is to combine a higher resolution modality, such as x-ray computed tomography (CT) or MRI to gain structural information, with a functional modality, such as DOT. In some studies, the structural details are used as *a priori* information to aid the optical reconstruction.^{11–13} In this article we compare DOT with positron emission tomography (PET), a clinically useful imaging modality that employs the uptake of radiopharmaceuticals such as fluorodeoxyglucose (^{18}F -FDG) to determine tissue metabolic activity. The increased metabolic rate of most tumors compared to normal tissue provides a basis for their detectability by ^{18}F -FDG PET.^{15–18}

Unlike x-ray computed tomography, ultrasound, and MRI, which are typically combined with DOT in order to provide anatomical structure, DOT and PET primarily measure physiological characteristics of tissue. Thus, the potential advantages of combining DOT and PET for breast imaging center largely on functional characterization. The ability to image tissue oxygen saturation (StO_2) in addition to ^{18}F -FDG uptake, for example, may provide insight about the relationship between glucose metabolism and hypoxia. Hypoxic tumors are often more resistant to therapy,^{19–21} and thus determination of tumor oxygenation status might afford improved disease management.^{22–25} Increased ^{18}F -FDG uptake is generally associated with hypoxia, because a lack of oxygen can lead to the anaerobic metabolism of glucose. However, some nonhypoxic tumors have high rates of glucose metabolism, and chronic hypoxia can lead to decreases in glucose metabolism. Thus ^{18}F -FDG PET alone is not a reliable measure of tissue hypoxia. This observation has led to recent research using nitroimidazole tracers such as ^{18}F -fluoromisonidazole to measure tumor hypoxia in variety of cancers including breast cancer.^{26,27}

Diffuse optical methods measure tissue oxygenation using endogenous contrast. Thus they are not subject to variations in tracer uptake due to physiological factors such as poor perfusion,²⁸ nor do they require the subject to return to the hospital another day for injection and scan of a second tracer. While the relationship between StO_2 and the partial pressure of oxygen (pO_2) is nonlinear and depends on other factors (e.g., pH, and temperature), the relationship is

monotonic, so that high/low values of StO_2 in a lesion with respect to the surrounding tissue imply corresponding high/low relative values of pO_2 . The relative rate of oxygen metabolism in tumors can also be probed by diffuse optical methods,²⁹ and might in the future provide a means to study the relationship between ^{18}F -FDG kinetics and oxygen metabolism. A high rate of glucose consumption without a high rate of oxygen metabolism would imply that some glucose is being metabolized inefficiently, presumably due to an insufficient supply of oxygen. In addition, co-registration of total hemoglobin concentration, blood oxygenation and glucose metabolism affords a method for increased tumor sensitivity and specificity compared to the stand-alone modalities based on changes of one tissue metabolic parameter.

It is reasonable to expect that increases in glucose metabolism require more blood for glucose and oxygen delivery, and therefore should be accompanied by increases in total hemoglobin concentration. In fact, ^{18}F -FDG uptake has already been shown to correlate well with the uptake of a tumor blood-flow-specific tracer in breast cancer.^{30,31} If a strong correlation between hemoglobin concentration and glucose consumption exists, it could have two major clinical consequences. First, PET will be well suited to validate DOT results. This is important because, unlike PET, DOT is still in its initial research phase and has not as yet been fully translated to the clinic. Second, DOT is a noninvasive and relatively low cost methodology, making it ideal for routine monitoring and widespread use. Several case studies along these lines have explored the use of optical methods to monitor neoadjuvant chemotherapy of locally advanced breast cancers.^{32–34} On the other hand, even though PET images after the first round of chemotherapy are demonstrably strong indicators of treatment efficacy in breast cancer patients,^{35–40} and PET scans after treatment can help predict clinical outcomes,^{41,42} these scans are expensive and require the administration of radioactive material, rendering them impractical for routine monitoring. If DOT and PET results are correlated, DOT's potential for breast cancer treatment monitoring would be enhanced.

In this study, the feasibility of multi-modal DOT and PET for breast cancer imaging is demonstrated for the first time. We co-register three-dimensional (3D) DOT images from three subjects with 3D PET images derived from a dedicated breast-only PET scanner. We also compare 3D DOT images from 14 subjects with results from corresponding whole-body PET images. Contrast in total hemoglobin concentration (THC), scattering (μ'_s), overall optical attenuation (μ_{eff}), and an optical index are found to correlate with contrast of ^{18}F -FDG uptake in whole-body PET images. Changes in tissue blood oxygenation (StO_2) are small and are uncorrelated with ^{18}F -FDG contrast in the whole-body PET images. Co-registered breast-only PET and DOT images tended to show THC, μ'_s , μ_{eff} , optical index, and ^{18}F -FDG contrast in the same spatial locations. However, with only three breast-only PET subjects, statistical correlations could not be made.

II. Methods

II.A. DOT instrumentation

Our DOT imaging device is a hybrid system. The instrument takes both continuous-wave transmission and frequency-domain remission measurements at six near-infrared wave-lengths in the parallel-plane soft-compression geometry. This device has been extensively characterized for use in breast imaging.^{1,32} We summarize its major features here.

The patient lies in a prone position with her breasts inside a box with an anti-reflection coated glass window on the detector side. A compression plate holds the breast in place against the viewing window by mildly compressing the breast to a thickness between 5.5 and 7.5 cm. The box is then filled with a matching fluid with optical properties similar to human breast. The matching fluid consists of water, india ink (Black India 4415, Sanford, Bellwood, IL) for

absorption, and a fat emulsion (Lyposyn III 30%, Abbott Laboratories, Chicago, IL) for scattering.

Six diode lasers (650, 690, 750, 786, 830, 905 nm), four of which (690, 750, 786, 830 nm) are intensity modulated at 70 MHz, are connected via optical fibers and series of optical switches (DiCon Fiber Optics, Richmond, CA) to 45 source positions located on the compression plate. The source positions form a 9×5 grid with a separation of 1.6 cm between nearest neighbors. The breast is scanned by serially guiding the light from each laser to each source position. A set of measurements for each laser/source-position combination is then obtained.

For remission detection, nine homodyne frequency domain detector units⁴³ are connected to the compression plate by a 3×3 grid of 3 mm detector fibers with a spacing of 1.6 cm. Each unit contains an avalanche photodiode, and utilizes a homodyne technique to derive the amplitude and phase of the detected signal. For transmission detection, a charge coupled device (CCD) camera (Roper Scientific, Trenton, NJ, VersArray:1300F) is focused on the viewing window. A 24×41 grid of 984 pixels is selected from the CCD chip. It measures the continuous wave light intensity at locations on the viewing window with a spacing of ~ 3 mm.

II.B. DOT image reconstruction

Our multi-spectral approach permits us to solve directly for oxy- and deoxy-hemoglobin concentrations via decomposition of the absorption coefficient into contributions from individual chromophores, assuming a simple Mie-scattering approximation for the reduced scattering coefficient. We implemented this approach by modifying TOAST (time-resolved optical absorption and scattering tomography) software in order to utilize multi-spectral continuous wave data.⁴⁴ Since our algorithm has already been reported,⁴⁵ we briefly summarize the method here.

The propagation of near-infrared light in biological media is modeled by a diffusion equation.⁹ In the frequency domain, the equation has the form

$$-\nabla \cdot D(r, \lambda) \nabla \Phi(r, \lambda, \omega) + \left[\mu_a(r, \lambda) + \frac{i\omega n}{c} \right] \Phi(r, \lambda, \omega) = q_o(r, \lambda, \omega). \quad (1)$$

Here Φ is the photon fluence rate, λ is the wavelength of light source, ω is the frequency at which the light source is intensity modulated ($\omega=0$ for continuous wave measurements), q_o is the light source distribution, and c is the speed of light. The optical properties of the breast are described by the light diffusion coefficient $D \approx 1/3\mu'_s$ (μ'_s is the reduced scattering coefficient), the absorption coefficient μ_a , and the tissue index of refraction n .

We model the absorption coefficient as sum of the absorption from the individual chromophores (Hb, HbO₂, water, and lipids) in the breast, i.e.,

$$\mu_a(\lambda) = \sum_i c_i \epsilon_i(\lambda). \quad (2)$$

Here c_i is the concentration of the i th chromophore, and $\epsilon_i(\lambda)$ is the corresponding wavelength dependent extinction coefficient.

We model the wavelength dependence of the reduced scattering coefficient using simplified Mie-scattering theory.^{46,47} A scattering prefactor A depends primarily on the number and size of scatterers, and a scattering exponent b depends on the size of the scatterers. They are combined as follows:

$$\mu'_s = A\lambda^{-b}. \quad (3)$$

Our strategy is to reconstruct spatial maps of A , b , and the chromophore concentrations, by minimizing the difference between measured data and predictions of the diffusion model.

Two scans are made for each breast: a reference scan in which the tank is filled with matching fluid only, and a scan with the breast immersed in matching fluid. We fit data from the frequency domain measurements of the breast to an analytic solution of the diffusion equation for a homogeneous medium in the slab geometry to obtain estimates of the average chromophore concentrations, scattering prefactor A , and scattering power b inside the breast. The absorption due to volume concentrations of water (31%) and lipid (57%) in the breast is held fixed, based on values from the literature.^{48–50} The optical properties of the matching fluid are determined independently by fitting the frequency domain measurements of the reference scan.

A photograph of the compressed breast is taken just before the scan. It allows us to segment the imaging volume into breast and matching fluid regions. Using average results for the breast as an initial guess, we then employ a nonlinear conjugate gradient algorithm to solve directly for 3D tomographic maps of the chromophore concentrations and scattering prefactor A inside the breast. The scattering amplitude b is held fixed at its bulk value, as are the optical properties of the matching fluid region. At each iteration, a finite element solver predicts the detected continuous wave light intensity based on the current maps of chromophore concentrations, and these maps are then updated in order to minimize a χ^2 which represents the difference between measured and predicted values of light exiting the breast. Finally, the resulting maps are combined to form images of total hemoglobin concentration [$\text{THC}(\mathbf{r}) = C_{\text{Hb}}(\mathbf{r}) + C_{\text{HbO}_2}(\mathbf{r})$], blood oxygen saturation, [$\text{StO}_2(\mathbf{r}) = C_{\text{HbO}_2}(\mathbf{r}) / \text{THC}(\mathbf{r})$], reduced scattering coefficient [$\mu'_s(r) = A(r)\lambda^{-b}$], overall optical attenuation [$\mu_{\text{eff}}(r) = \sqrt{\mu_a(r)/D(r)}$], and an empirical optical index [$OI(r) = r\text{THC}(r) \times r\mu'_s(r) / r\text{StO}_2(r)$].

II.C. Whole-body PET

Commercially available whole-body PET tomographs achieve high sensitivity to 511 KeV annihilation photon pairs using a cylindrical configuration of detectors surrounding the patient. The imaging instrument used for acquisition of whole-body PET images in this study was an Allegro scanner (Philips Medical Systems), with an axial field of view (FOV) of 18 cm, a trans-axial FOV of 56 cm, and a ring diameter of 86.4 cm at the surface of the detectors. The scanner exhibits 5 mm spatial resolution (i.e. full width at half maximum of a point source), and a sensitivity of 4.4 cps/kBq.⁵¹

Patients fasted for at least 4 h prior to the scan. Each scan was initiated 60 min after intravenous administration of ^{18}F -FDG with a dose of 5.2 MBq/kg. Sequential overlapping scans were acquired to cover the body from neck to pelvis, as the patient lay supine on the bed. Transmission scans obtained with a ^{137}Cs point source were interleaved between the multiple emission scans to correct for nonuniform attenuation of the 511 KeV photons by the patients body and the bed.

The detected photon-pair events were reconstructed to produce an image using a fully 3D iterative reconstruction technique, the row-action maximum likelihood algorithm (3D RAMLA).⁵² This algorithm includes correction for attenuation in the system model. Scatter and randoms correction are performed in addition to produce quantitative images.

II.D. Breast-only PET

The ability to image breast cancer with ^{18}F -FDG PET has led to the development of a dedicated breast imaging PET scanner, BPET.^{53,54} In a whole-body scanner, the 511 KeV photons emitted from the breast are attenuated by the body, reducing the scanner's sensitivity to breast lesions. In contrast, a dedicated breast scanner permits the breast to be imaged with significant reduction in attenuation, i.e., by about a factor of 10. As with the DOT device, the woman lies prone on a table with an opening to allow the breast to drop between two detectors whose separation distance can be adjusted to accommodate different sized breasts.

The scanner is composed of two curved plate NaI(Tl) detectors of 1.9 cm thickness each with an active area of $28 \times 21 \text{ cm}^2$. By positioning the detectors close to the breast, a large solid angle can be covered, optimizing the system's sensitivity for a split ring configuration. However, this configuration leads to the loss of data from the 511 KeV photons arriving at angles not covered by the detector plates. In fact, for a typical separation of 20 cm the angular coverage of 180° corresponds to 1/2 of complete angular acceptance. This geometry requires the use of a limited angle reconstruction which we perform using a modified version of 3D RAMLA that compensates for the missing data.

The spatial resolution of the system varies from 3.8 mm (radially at center) to 4.5 mm (radially at $r=5 \text{ cm}$) in comparison to uniform 5 mm for the Allegro scanner. Phantom measurements have demonstrated superior contrast recovery for BPET compared to Allegro as a result of the improved spatial resolution, despite the loss of data due to the limited angle geometry. In addition, a pilot study of 20 patients imaged with both Allegro and BPET demonstrated good correlation in lesion detectability, but overall better detail in the breast lesions was achieved in the BPET images.⁵⁵

II.E. Subject protocol

Informed consent was given by all DOT and BPET patients in accordance with the University of Pennsylvania Institutional Review Board. Out of the 30 patients who received both DOT and whole-body PET scans, we selected the 14 who had not received a biopsy or any form of treatment between the dates of the DOT and PET scans. For 12 of these patients, the two scans were on the same day. For the other two, the scans were separated by four and 13 days.

To date, three of the 30 patients have also been successfully scanned with our prototype BPET instrument in addition to receiving the whole-body PET scan. The geometries of the DOT and BPET instruments are similar, with the patient lying prone with sources/detectors towards the head and feet, allowing us to co-register the images using a deformation algorithm (see Sec. V). Unfortunately, two of these patients received core biopsies between the DOT and BPET measurements. Nevertheless, given the potential advantages of co-registering the images, we include results for all three BPET patients in this preliminary study.

II.F. Image co-registration

Co-registration of DOT and BPET images makes possible comparison of specific regions of the BPET images with their corresponding regions in DOT images. Co-registration also enables one to determine to what extent lesions appear in the same spatial locations for the two modalities. Although the images were acquired with separate stand-alone scanners, the similar geometries of the scanners made co-registration possible, though the problem was made more challenging because the breast hangs freely in the BPET scanner, while in the DOT scanner, the breast is mildly compressed (to a thickness between 5.5 and 7.5 cm).

The 3D-DOT/3D-PET image registration presents new challenges and there is no standard of co-registration today to validate against. We have conducted initial patient and phantom

validation studies^{56–59} for 3D-DOT/3D-MR image registration which confirm the accuracy of our algorithm. The method is automatic with little prior user interaction required. It is robust enough to handle a majority of patient cases and computationally efficient for practical applicability. We briefly review the major features of the registration algorithm below.

The DOT images are reconstructed on finite element meshes containing on average 50 000 nodes and 200 000 tetrahedral elements. Each node is associated with a set of reconstructed physiological parameters (e.g., THC, StO₂, and μ'_s). To facilitate registration of DOT to PET images, we first determine these physiological values on a 3D voxelized sample volume. Each voxel is given an interpolated value calculated from the shape functions within the tetrahedral element that contains the center point of that specific voxel.

Once the DOT image has been interpolated onto the voxels, it is co-registered with the PET image using a combination of the methods demonstrated in Refs. 60 and 61. First we compute two-dimensional (2D) projection images for both the DOT and PET images. Second, we define a similarity measure⁶² to compute the amount of mutual information between the 2D DOT and PET projections. We then maximize this measure by warping the DOT image volume. An optimization scheme searches through a nine-dimensional parameter space consisting of rigid body motion (translation and rotation), and independent linear scaling in all three dimensions. In this way, the projection images are registered within a 2D space, which is a subset of the 3D space of the original registration transformations. We perform these registrations successively for three mutually orthogonal projection geometries in order to estimate all registration parameters. We further optimize the performance of projection and 2D-2D registration similarity computation using graphics processing units. A general validation of our approach can be found in Ref. 63.

Figure 1 shows cross sections of a 3D reconstructed breast image before and after co-registration. The reconstructed image shown in the left column corresponds to the actual DOT measurement geometry in which the breast is compressed axially. The right column shows the same reconstructed image after being co-registered by the volume warping algorithm. Once the co-registration was completed, the location of the lesion was determined by looking at the BPET image. An ellipsoidal volume corresponding to the lesion was chosen as the region of interest (ROI), and this exact same ROI was selected in the DOT images.

The situation with whole-body PET is different. During whole-body PET scans, the patient lies in a supine position, as opposed the prone position of the DOT and BPET scanners. In the supine position, the breast is compressed against the chest, and deforms unpredictably. Generally, rigid body motion and linear scaling cannot account for all of these deformations. As a result, when comparing DOT images to those from *whole-body* PET scans we are unable to co-register the images.

III. Results

III.A. DOT and BPET Results

Axial slices from the co-registered images of the three patients receiving both DOT and BPET scans appear in Fig. 2. Regions of interest determined from the PET images are denoted by dashed ellipses.

Subject A had a suspicious mass in her right breast. A core biopsy performed five weeks before DOT and BPET imaging revealed a ductal carcinoma *in situ*, with some evidence of invasive carcinoma as well. Biopsy marks were still visible the day imaging was performed. Digital mammography and MRI (performed the same day as DOT and BPET) saw some enhancement, while ultrasound (also the same day) had no suspicious findings. The BPET image shows

increased FDG uptake above the nipple. The DOT images show an increase in THC, μ'_s , μ_{eff} , and optical index in this same location. A subsequent biopsy indicated that ductal carcinoma *in situ* was still present on the day the imaging was performed.

Subject B had a palpable mass in the subareolar region of the left breast. The mass (~3 cm across) was visible to both x-ray CT and ultrasound. DOT images indicate an increase in THC, μ'_s , μ_{eff} , and optical index at the location of the mass, as well as a decrease in StO₂ slightly above this region. An excisional biopsy of the mass (performed later during the same day as the DOT exam) revealed a hemorrhage in its center, consistent with the increase in THC seen by DOT. The lesion was diagnosed as a partially organized abscess with no carcinoma present. BPET was performed 11 days later. The increase in FDG uptake was due to a postsurgical seroma. This collection of serous fluid was located in the same position as the mass which was removed.

Subject C had multiple masses of concern. A core biopsy revealed invasive ductal carcinoma. BPET was performed about a month before the biopsy. FDG uptake is clearly visible. Unfortunately, DOT was not performed until one month after the biopsy (i.e., two months after BPET). Most notable in the DOT image, is an increase in THC, μ'_s , μ_{eff} , and optical index along with a decrease in StO₂ in the region above the nipple. A subsequent excisional biopsy showed that invasive ductal carcinoma was still present at the location of the original biopsy at the time of the DOT measurement.

The co-registered images in Fig. 2 show qualitatively that DOT parameters (with the exception of StO₂) are above average in the ROIs determined from BPET. To quantify this observation, we performed the following analysis. For each DOT image, we calculate the average value of particular image parameters for all voxels in the entire breast and for all voxels in the ROI. The tumor-to-background ratio (TBR) is defined as the ratio between these two values. Results are shown in Table I. The optical index parameter shows the greatest contrast (TBR=1.5–1.7).

THC, μ'_s , and μ_{eff} exhibit somewhat less contrast (TBR=1.1–1.4), while very little variation in StO₂ is observed (TBR \cong 1.0).

III.B. DOT and whole-body PET results

In this preliminary study, we compared lesions that were visible in both DOT and PET, without trying to classify them as cancerous or benign based on imaging alone. Out of the 14 subjects measured, contrast was visible in both DOT and PET images for nine subjects, neither DOT nor PET for two subjects, and PET only for three subjects. When contrast was seen in the DOT images it always appeared in THC, μ'_s , μ_{eff} , and optical index. Significant contrast was never observed in StO₂. Representative images from a patient with invasive ductal carcinoma are shown in Fig. 3.

We compared these results with the pathology reports from biopsies taken after imaging. A summary of the results is found in Table II. Of the nine subjects who showed both DOT and PET contrast, histopathology confirmed invasive ductal carcinoma (IDC) with ductal carcinoma *in situ* (DCIS) in seven subjects, DCIS only in one subject, and normal breast tissue in one subject. In one of the subjects with IDC, two distinct lesions were visible with PET, but only the larger one was visible with DOT. For the subject with normal breast tissue, the increase in FDG uptake was located at a previous surgical site, and was due to a post-excisional inflammation. This inflammation was visible in the DOT images as well. Of the two subjects who showed neither DOT or PET contrast, one had a possible lipoma (benign), and the other had a cyst. Of the three subjects who showed contrast in PET but not in DOT, one had IDC and DCIS, one had a cyst (superficial and probably infected), and one did not receive a biopsy

after negative findings from both ultrasound and MRI. For this subject, the uptake of FDG was diffuse, i.e., no clear focus of FDG uptake was visible.

We also made a quantitative comparison of the tumor-to-background ratio (TBR) in the DOT and whole-body PET images. For each image, we identified the voxel in the tumor region with the maximum value. The corresponding ROI consisted of a 1-cm-diameter circular region around this pixel. Correlations between contrast ratios in FDG and DOT are shown in Fig. 4. A positive correlation (p value <0.05) was found between FDG uptake and THC, μ'_s , μ_{eff} , and optical index. However, correlation coefficients for these parameters were not particularly high ($R=0.67-0.76$). In addition to calculating contrast ratios, we also determined the mean and maximum standardized uptake values (SUVs) for the PET scans. We found that use of SUVs, as opposed to contrast ratios, had little effect on the correlations with DOT parameters. We also compared tumor-to-background ratio variation with age, tumor grade, and tumor size. Significant correlations were not found.

IV. Discussion

Our reconstructed DOT images show increases in both total hemoglobin concentration and scattering at tumor locations. Furthermore, the initial DOT/PET comparisons demonstrate these enhancements are located in approximately the same spatial locations (as shown by co-registering BPET images) and are correlated in intensity (as shown by analysis with whole-body PET images.) The principle source of the scattering of near-infrared light in tissue is believed to come from cellular organelles, particularly mitochondria. Since mitochondria are responsible for cellular metabolism, it is perhaps not surprising that an increase in glucose metabolism as measured by FDG uptake would be accompanied by an increase in the scattering of near-infrared light. One might also expect increases in FDG uptake to be accompanied by increases in blood volume to help supply tumors that have high metabolic rates. Recently Semple *et al.* explored the relationship between vascular and metabolic characteristics of primary breast tumors using FDG PET and dynamic contrast-enhanced MRI.⁶⁴ Their findings suggest the amount of FDG uptake is affected by the vascular characteristics of the tumor. It is also possible that there is some absorption-scatter image cross-talk in the DOT images due to the fact the wave-lengths used in our DOT scanner are not optimal for separating THC from μ'_s in the reconstructed images.⁴⁵ However, our 3D simulations with noise in the same geometry have cross-talk of less than 20% between THC and scattering. Thus, although there remains some quantitative uncertainties about the relative contributions of THC and μ'_s contrast to our DOT reconstructed images, the results clearly demonstrate that the increase in overall optical attenuation μ_{eff} and optical index, due to the combination of absorption and scattering, is closely linked to the uptake of FDG.

In contrast to scattering and total hemoglobin concentration, StO_2 showed little contrast. This result casts doubt on one of the long-range motivations for this study, i.e., use of DOT and PET to examine the relationship between glucose metabolism and tumor oxygen status. We note, however, that the numbers of patients examined here are small, and the situation might be quite different for different tumor types or tissue disease.

In order to determine if a lesion was visible in a DOT image, we first consulted the radiologists' reports from other imaging modalities (x-ray mammogram, ultrasound, MRI, and PET) to define the approximate location of the lesion. We then made a visual assessment of whether there was a change in that area of the breast. Whenever a change was visible, it occurred as an increase in both THC and scattering (and thus μ_{eff} and optical index as well). We did not see significant changes in tissue blood oxygenation (StO_2) for any patients.

In this study we compared DOT and PET images with results from pathology. However, since predicting the outcome of treatment is a major potential of metabolic imaging, future studies will be needed to monitor therapy and track the final clinical outcomes for patients. In order to learn what factors influence the degree of correlation between glucose metabolism and DOT parameters, a larger group of patient volunteers will be needed.

V. Conclusion

We compared reconstructed DOT breast images with images from both a commercial whole-body PET scanner, and a prototype breast-only PET scanner. The similarity of acquisition geometries between the DOT and breast-only PET scanners made it possible to co-register images from the two separate scanners by deforming the DOT image with a volume warping algorithm. This scheme permitted us to compare images at specific locations. Images acquired with both PET scanners showed a correspondence between FDG uptake and DOT parameters. Comparison with breast-only PET demonstrated similar spatial locations of lesions, whereas whole-body PET demonstrated a correlation in tumor contrast. To our knowledge these are the first direct comparisons of DOT and PET images for breast cancer. The work demonstrates the feasibility of this multi-modal approach.

Acknowledgements

The authors thank J. P. Culver for his initial work on the optical instrumentation, M. Grosicka-Koptyra for patient recruitment and measurement, and M. D. Schnall, M. A. Rosen, B. J. Czerniecki, and J. C. Tchou for patient recruitment. This research was supported by Grant Nos. NIH R01-CA75124, NIH R01 EB-002109, NTR01 IU54CA105480, NIH P01-CA85424, and DOE DE-FG02-88ER60642.

References

1. Culver JP, Choe R, Holboke MJ, Zubkov L, Durduran T, Slemp A, Ntziachristos V, Chance B, Yodh AG. Three-dimensional diffuse optical tomography in the parallel plane transmission geometry: Evaluation of a hybrid frequency domain/continuous wave clinical system for breast imaging. *Med Phys* 2003;30:235–247. [PubMed: 12607841]
2. Pogue BW, Poplack SP, McBride TO, Wells WA, Osterman KS, Osterberg UL, Paulsen KD. Quantitative hemoglobin tomography with diffuse near-infrared spectroscopy: Pilot results in the breast. *Radiology* 2001;218:261–266. [PubMed: 11152812]
3. Ntziachristos V, Chance B. Probing physiology and molecular function using optical imaging: Applications to breast cancer. *Breast Cancer Res* 2001;3:41–46. [PubMed: 11250744]
4. Gu XJ, Zhang QZ, Bartlett M, Schutz L, Fajardo LL, Jiang HB. Differentiation of cysts from solid tumors in the breast with diffuse optical tomography. *Acad Radiol* 2004;11:53–60. [PubMed: 14746402]
5. Pifferi A, Taroni P, Torricelli A, Messina F, Cubeddu R, Danesini G. Four-wavelength time-resolved optical mammography in the 680–980 nm range. *Opt Lett* 2003;28:1138–1140. [PubMed: 12879933]
6. Grosenick D, Wabnitz H, Moesta KT, Mucke J, Moller M, Stroszczyński C, Stossel J, Wassermann B, Schlag PM, Rinneberg H. Concentration and oxygen saturation of haemoglobin of 50 breast tumours determined by time-domain optical mammography. *Phys Med Biol* 2004;49:1165–1181. [PubMed: 15128196]
7. Schmitz C, Klemer D, Hardin R, Katz M, Pei Y, Graber H, Levin M, Levina R, Franco N, Solomon W, Barbour R. Design and implementation of dynamic near-infrared optical tomographic imaging instrumentation for simultaneous dual-breast measurements. *Appl Opt* 2005;44:2140–2153. [PubMed: 15835360]
8. Pera VE, Heffer EL, Siebold H, Schutz O, Heywang-Kobrunner S, Gotz L, Heinig A, Fantini S. Spatial second-derivative image processing: An application to optical mammography to enhance the detection of breast tumors. *J Biomed Opt* 2003;8:517–524. [PubMed: 12880359]
9. Yodh, AG.; Boas, DA. Functional imaging with diffusing light. In: Vo-Dinh, T., editor. *Biomedical Photonics Handbook*. CRC; Boca Raton: 2003. p. 21-1.p. 21-45.

10. Ntziachristos V, Ma XH, Chance B. Time-correlated single photon counting imager for simultaneous magnetic resonance and near-infrared mammography. *Rev Sci Instrum* 1998;69:4221–4233.
11. Hsiang D, Shah N, Yu H, Su M, Cerussi A, Butler J, Baick C, Mehta R, Nalcioglu O, Tromberg B. Coregistration of dynamic contrast enhanced MRI and broadband diffuse optical spectroscopy for characterizing breast cancer. *Technol Cancer Res Treat* 2005;4:549–58. [PubMed: 16173825]
12. Brooksby B, Pogue BW, Jiang S, Dehghani H, Srinivasan S, Kogel C, Tosteson TD, Weaver J, Poplack SP, Paulsen KD. Imaging breast adipose and fibroglandular tissue molecular signatures using hybrid mri-guided near-infrared spectral tomography. *Proc Natl Acad Sci USA* 2006;103:8828–8833. [PubMed: 16731633]
13. Zhu QI, Huang MM, Chen NG, Zarfos K, Jagjivan B, Kane M, Hedge P, Kurtzman SH. Ultrasound-guided optical tomographic imaging of malignant and benign breast lesions: Initial clinical results of 19 cases. *Neoplasia* 2003;5:379–388. [PubMed: 14670175]
14. Li A, Miller EL, Kilmer ME, Brukilacchio TJ, Chaves T, Stott J, Zhang Q, Wu T, Chorlton M, Moore RH, Kopans DB, Boas DA. Tomographic optical breast imaging guided by three-dimensional mammography. *Appl Opt* 2003;42:5181–5190. [PubMed: 12962399]
15. Karp JS, Freifelder R. Current and future technological trends in positron emission tomography. *J Neuroimaging* 1992;2:102–110. [PubMed: 10150075]
16. Avril N, Dose J, Janicke F, Bense S, Laubenbacher ZSC, Romer W, Pache H, Herz M, Allgayer B, Nathrath W, Graeff H, Schwaiger M. Metabolic characterization of breast tumors with positron emission tomography using F-18 fluorodeoxyglucose. *J Clin Oncol* 1996;14:1848–1857. [PubMed: 8656253]
17. Avril N, Rose CA, Schelling M, Dose J, Kuhn W, Bense S, Weber W, Ziegler S, Graeff H, Schwaiger M. Breast imaging with positron emission tomography and fluorine-18 fluorodeoxyglucose: Use and limitations. *J Clin Oncol* 2000;42:3495–3502. [PubMed: 11032590]
18. Avril N, Menzel M, Dose J, Schelling M, Weber W, Janicke F, Nathrath W, Schwaiger M. Glucose metabolism of breast cancer assessed by 18F-FDG PET: Histologic and immunohistochemical tissue analysis. *J Nucl Med* 2001;42:9–16. [PubMed: 11197987]
19. Emmenegger U, Morton GC, Francia G, Shaked Y, Franco M, Weinerman A, Man S, Kerbel RS. Low-dose metronomic daily cyclophosphamide and weekly tirapazamine: A well-tolerated combination regimen with enhanced efficacy that exploits tumor hypoxia. *Cancer Res* 2006;66:1664–1674. [PubMed: 16452226]
20. Warenus HM, White R, Peacock JH, Hanson J, Britten RA, Murray D. The influence of hypoxia on the relative sensitivity of human tumor cells to 62.5 MeV (p to Be) fast neutrons and MeV photons. *Radiat Res* 2000;154:54–63. [PubMed: 10856966]
21. Vaupel P, Hockel M. Blood supply, oxygenation status and metabolic micromilieu of breast cancers: Characterization and therapeutic relevance (Review). *Int J Oncol* 2000;17:869–879. [PubMed: 11029486]
22. Hockel M, Vaupel P. Tumor hypoxia: Definitions and current clinical, biologic, and molecular aspects. *J Natl Cancer Inst* 2001;93:266–276. [PubMed: 11181773]
23. Blagosklonny MV. Hypoxia-inducible factor: Achilles heel of antiangiogenic cancer therapy. *Int J Oncol* 2001;19:257–262. [PubMed: 11445836]
24. Moeller BJ, Cao Y, Vujaskovic Z, Li CY, Haroon ZA, Dewhirst MW. The relationship between hypoxia and angiogenesis. *Semin Radiat Oncol* 2004;14:215–221. [PubMed: 15254864]
25. Denny WA. Prospects for hypoxia-activated anticancer drugs. *Curr Med Chem Anti-Canc Agents* 2004;4:395–399.
26. Rajendran J, Mankoff D, O'Sullivan F, Peterson L, Schwartz D, Conrad E, Spence A, Muzi M, Farwell D, Krohn K. Hypoxia and glucose metabolism in malignant tumors evaluation by [18F] fluoromisonidazole and [18F] fluorodeoxyglucose positron emission tomography imaging. *Clin Cancer Res* 2004;10:2245–2252. [PubMed: 15073099]
27. Padhani A, Krohn K, Lewis J, Alber M. Imaging oxygenation of human tumours. *Eur Radiol* 2007;17:861–872. [PubMed: 17043737]
28. Thorwarth D, Eschmann S, Paulsen F, Alber M. A kinetic model for dynamic [18F]-Fmiso PET data to analyze tumor hypoxia. *Phys Med Biol* 2005;50:2209–2224. [PubMed: 15876662]

29. Zhou C, Choe R, Shah N, Durduran T, Yu GQ, Durkin A, Hsiang D, Mehta R, Butler J, Cerussi A, Tromberg BJ, Yodh AG. Diffuse optical monitoring of blood flow and oxygenation in human breast cancer during early stages of neoadjuvant chemotherapy. *J Biomed Opt* 2007;12:051903. [PubMed: 17994886]
30. Zasadny KR, Tatsumi M, Wahl RL. FDG metabolism and uptake versus blood flow in women with untreated primary breast cancers. *Eur J Nucl Med Mol Imaging* 2003;30:274–280. [PubMed: 12552346]
31. Tseng J, Dunnwald LK, Schubert EK, Link JM, Minoshima S, Muzi M, Mankoff DA. 18F-FDG kinetics in locally advanced breast cancer: Correlation with tumor blood flow and changes in response to neoadjuvant chemotherapy. *J Nucl Med* 2004;45:1829–1837. [PubMed: 15534051]
32. Choe R, Corlu A, Lee K, Durduran T, Konecky SD, Grosicka-Koptyra M, Arridge SR, Czerniecki BJ, Fraker DL, DeMichele A, Chance B, Rosen MA, Yodh AG. Diffuse optical tomography of breast cancer during neoadjuvant chemotherapy: A case study with comparison to MRI. *Med Phys* 2005;32:1128–1139. [PubMed: 15895597]
33. Jakubowski DB, Cerussi AE, Bevilacqua F, Shah N, Hsiang D, Butler J, Tromberg BJ. Monitoring neoadjuvant chemotherapy in breast cancer using quantitative diffuse optical spectroscopy: A case study. *J Biomed Opt* 2004;9:230–238. [PubMed: 14715078]
34. Zhu Q, Kurtzma SH, Hegde P, Tannenbaum S, Kane M, Huang M, Chen NG, Jagjivan B, Zarfos K. Utilizing optical tomography with ultrasound localization to image heterogeneous hemoglobin distribution in large breast cancers. *Neoplasia* 2005;7:263–270. [PubMed: 15799826]
35. Schwarz D, Bader M, Jenicke L, Hemminger G, Janicke F, N A. Early prediction of response to chemotherapy in metastatic breast cancer using sequential 18F-FDG PET. *J Nucl Med* 2005;46:1144–1150. [PubMed: 16000283]
36. Smith IC, Welch AE, Hutcheon AW, Miller ID, Payne S, Chilcott F, Waikar S, Whitaker T, Ah-See AK, Eremin O, Heys SD, Gilbert FJ, Sharp PF. Positron emission tomography using [(18)f]-fluorodeoxy-d-glucose to predict the pathologic response of breast cancer to primary chemotherapy. *J Clin Oncol* 2000;18:1676–1688. [PubMed: 10764428]
37. Wahl RL, Zasadny K, Helvie M, Hutchins GD, Weber B, Cody R. Metabolic monitoring of breast cancer chemohormonotherapy using positron emission tomography: Initial evaluation. *J Clin Oncol* 1993;11:2101–2111. [PubMed: 8229124]
38. Schelling M, Aril N, Nahrig J, Kuhn W, Romer W, Sattler D, Werner M, Dose J, Janicke F, Graeff H, Schwaiger M. Positron emission tomography using [f-18] fluorodeoxyglucose for monitoring primary chemotherapy in breast cancer. *J Clin Oncol* 2000;18:1689–1695. [PubMed: 10764429]
39. Mankoff DA, Dunnwald LK, Gralow JR, Ellis GK, Schubert EK, Tseng J, Lawton TJ, Linden HM, Livingston RB. Changes in blood flow and metabolism in locally advanced breast cancer treated with neoadjuvant chemotherapy. *J Nucl Med* 2003;44:1806–1814. [PubMed: 14602864]
40. Gennari A, Donati S, Salvadori BA. Role of 2-[18F]-fluorodeoxyglucose (FDG) positron emission tomography (PET) in the early assessment of response to chemotherapy in metastatic breast cancer patients. *Clin Breast Cancer* 2000;1:156–161. [PubMed: 11899654]
41. Cachin F, Prince HM, Hogg A, Ware RE, Hicks RJ. Powerful prognostic stratification by [18F] fluorodeoxyglucose positron emission tomography in patients with metastatic breast cancer treated with high-dose chemotherapy. *J Clin Oncol* 2006;24:3026–3031. [PubMed: 16717291]
42. Vranjesevic D, Filmont JE, Meta JA. Whole-body (18)F-FDG PET and conventional imaging for predicting outcome in previously treated breast cancer patients. *J Nucl Med* 2002;43:325–329. [PubMed: 11884491]
43. Yang YS, Liu HL, Li XD, Chance B. Low-cost frequency-domain photon migration instrument for tissue spectroscopy, oximetry, and imaging. *Opt Eng (Bellingham)* 1997;36:1562–1569.
44. [January, 2007]. <http://www.medphys.ucl.ac.uk/~martins/toast/index.html>
45. Corlu A, Choe R, Durduran T, Schweiger M, Hillman EMC, Arridge SR, Yodh AG. Diffuse optical tomography with spectral constraints and wavelength optimization. *Appl Opt* 2005;44:2082–2093. [PubMed: 15835357]
46. Bevilacqua F, Berger A, Cerussi A, Jakubowski D, Tromberg B. Broadband absorption spectroscopy in turbid media by combined frequency-domain and steady-state methods. *Appl Opt* 2000;39:6498–6507. [PubMed: 18354663]

47. Mourant J, Fuselier T, Boyer J, Johnson T, Bigio I. Predictions and measurements of scattering and absorption over broad wavelength ranges in tissue phantoms. *Appl Opt* 1997;36:949–957. [PubMed: 18250760]
48. Woodard HQ, White DR. The composition of body tissues. *Br J Radiol* 1986;59:1209–1219. [PubMed: 3801800]
49. White DR, Woodard HQ, Hammond SM. Average soft-tissue and bone models for use in radiation dosimetry. *Br J Radiol* 1987;60:907–913. [PubMed: 3664185]
50. Lee NA, Rusinek H, Weinreb JC, Chandra R, Singer RC, Newstead GM. Fatty and fibroglandular tissue volumes in the breasts of women 20–83 years old: Comparison of x-ray mammography and computer-assisted MR imaging. *AJR Am J Roentgenol* 1997;168:501–506. [PubMed: 9016235]
51. Surti S, Karp J. Imaging characteristics of a 3-D GSO whole-body PET camera. *J Nucl Med* 2004;45:1040–1049. [PubMed: 15181139]
52. Daube-Witherspoon ME, Matej S, Karp JS, Lewitt RM. Application of the row action maximum likelihood algorithm with spherical basis functions to clinical PET imaging. *IEEE Trans Nucl Sci* 2001;48:24–30.
53. Freifelder R, Karp JS. Dedicated PET scanners for breast imaging. *Phys Med Biol* 1997;42:2453–2480.
54. Freifelder, R.; Cardi, C.; Grigoras, I.; Saffer, JR.; Karp, JS. First results of a dedicated breast PET imager, BPET, using NaI(Tl) curve plate detectors. *IEEE Nuclear Science Symposium Conference Record*; 2001. p. 1241-1245.
55. Srinivas, S.; Freifelder, R.; Saffer, J.; Cardi, C.; Geagan, M.; Werner, M.; Kent, A.; Alavi, A.; Schnall, M.; Karp, J. A dedicated breast positron emission tomography (B-PET) scanner: Characterization and pilot patient study. *IEEE Nuclear Science Symposium and Medical Imaging Conference Record*; San Diego CA. 2006.
56. Azar F, Lee K, Khamene A, Choe R, Corlu A, Konecky S, Sauer F, Yodh A. Standardized platform for coregistration of non-concurrent diffuse optical and magnetic resonance breast images obtained in different geometries. *J Biomed Opt* 2007;12:051902. [PubMed: 17994885]
57. Azar, FS.; Hajjioui, N.; Khamene, A.; Grady, L.; Lee, K.; Choe, R.; Corlu, A.; Konecky, SD.; Yodh, AG.; Sauer, F. A software platform for visualization and multimodal registration of diffuse optical tomography and MRI of breast cancer. In: Azar, FS.; Metaxas, MN., editors. *Multimodal Biomedical Imaging*. 6801. SPIE; Bellingham: 2006. p. 60810L
58. Azar, FS.; ElBawab, M.; Khamene, A.; Lee, K.; Choe, R.; Corlu, A.; Konecky, SD.; Yodh, AG.; Sauer, F. Multimodal information integration and visualization: Optical imaging and MRI. In: Analoui, M.; Dunn, DA., editors. *Optical Methods in Drug Discovery and Development*. 6009. SPIE; Bellingham: 2005. p. 60090E
59. Azar FS, ElBawab M, Khamene A, Lee K, Choe R, Corlu A, Konecky SD, Yodh AG, Sauer F. Multimodal 3D registration of non-concurrent diffuse optical tomography with MRI of breast cancer. *Society for Molecular Imaging*, Cologne, Germany. 2005
60. Cain SC, Hayat MM, Armstrong EE. Projection-based image registration in the presence of fixed-pattern noise. *IEEE Trans Image Process* 2001;10:1860–1872. [PubMed: 18255526]
61. Chan, H.; Chung, ACS. Efficient 3D-3D vascular registration based on multiple orthogonal 2D projections. In: Gee, JC.; Maintz, JBA.; Vannier, MW., editors. *Biomedical Image Registration: Second International Workshop, WBIR 2003*; Philadelphia, PA. June 23–24, 2003; WBIR; 2003. p. 301-310. Revised Papers
62. Wells WM, Viola P, Atsumi H, Nakajima S, Kikinis R. Multimodal volume registration by maximization of mutual information. *Med Image Anal* 1996;1:35–51. [PubMed: 9873920]
63. Khamene, A.; Chisu, R.; Wein, W.; Navab, N.; Sauer, F. A novel projection based approach for medical image registration. In: Plum, JPW.; Likar, B.; Gerritsen, FA., editors. *Biomedical Image Registration: Third International Workshop, WBIR 2006*; Utrecht, The Netherlands. July 9–11, 2006; 2006. Proceedings
64. Semple SIK, Gilbert FJ, Redpath TW, Staff RT, Ahearn TS, Welch AE, Heys SD, Hutcheon AW, Smyth EH, Chaturvedi S. The relationship between vascular and metabolic characteristics of primary breast tumours. *Eur Radiol* 2004;14:2038–2045. [PubMed: 15316743]

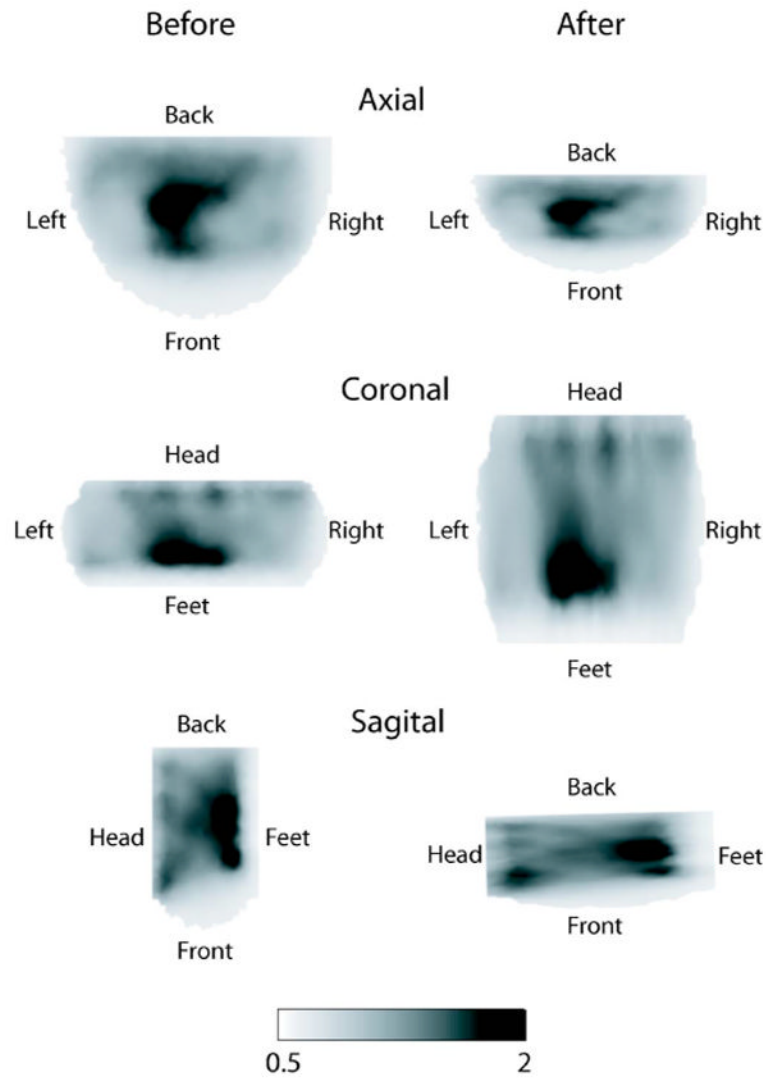


Fig. 1. Cross-sections of the 3D reconstructed image of optical index for patient A. Left and right columns correspond to before and after image co-registration. Rows correspond to axial, coronal, and sagittal views of the breast.

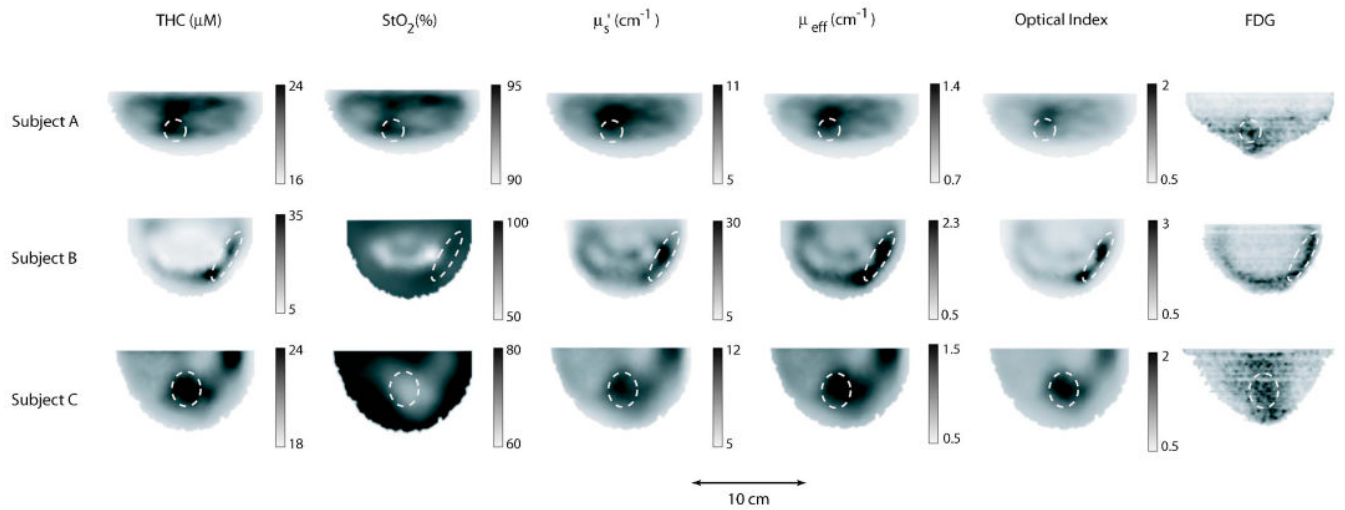


Fig. 2.

Images of the breasts from three females imaged with both DOT and BPET. Each image corresponds to a caudal-cranial slice taken from the 3D reconstruction of a breast after co-registration. Each row corresponds to a breast from one of the three patients. The columns correspond to total hemoglobin concentration (THC), tissue blood oxygenation (StO_2), reduced scattering coefficient μ'_s at 786 nm, overall attenuation (μ_{eff}), optical index, and FDG uptake measured with PET. The dashed ellipses enclose the regions of interest.

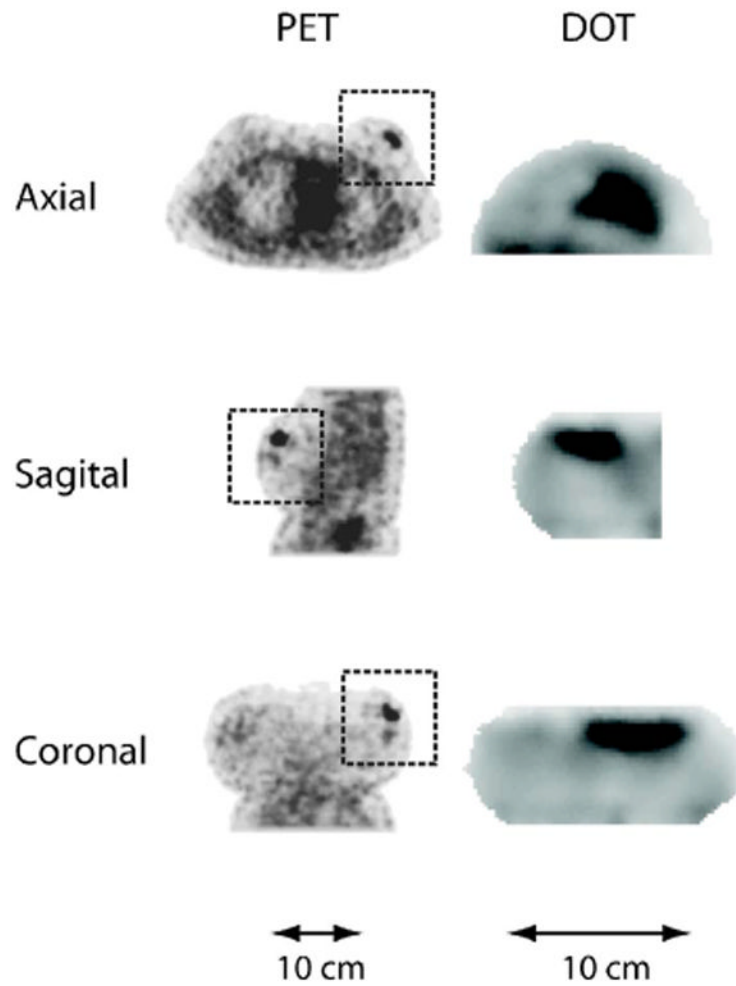
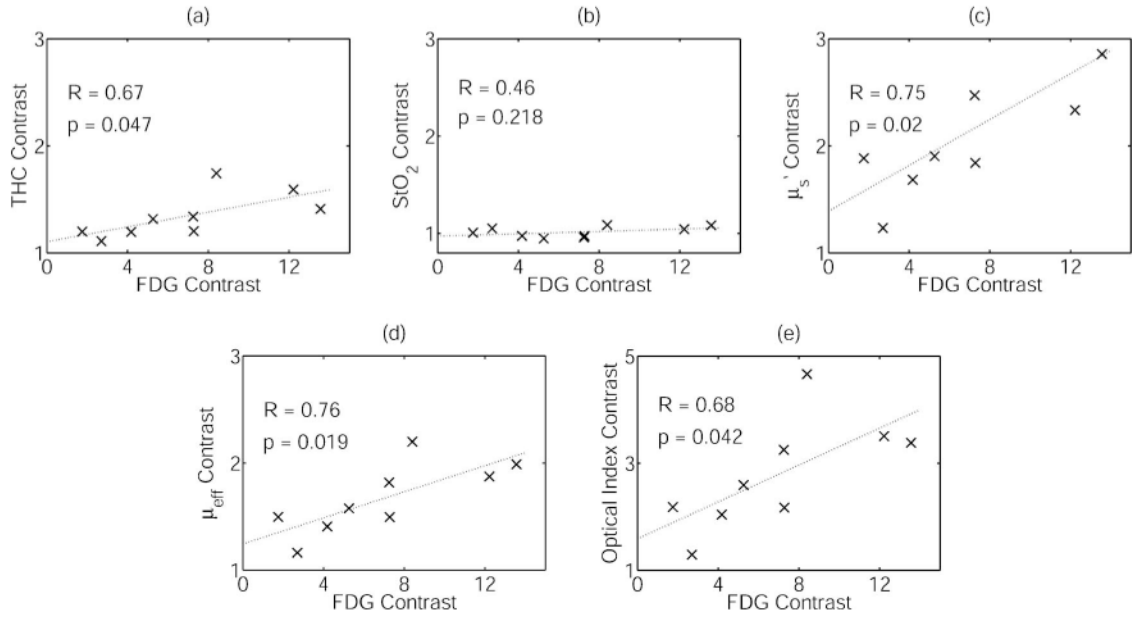


Fig. 3. Axial, sagittal, and coronal slices from the PET (FDG) and DOT (μ_{eff}) reconstructed images of subject 4. The orientation for the PET and DOT images is the same. However, the DOT images are of the left breast only, whereas the entire torso is shown in the PET images. Rectangular boxes denote the breast region in the whole-body PET images.

**Fig. 4.**

Correlations between contrast ratios in FDG uptake and DOT parameters for the nine patients with tumors visible to both DOT and PET. R and p denote the correlation coefficient and p value, respectively. (a) Total hemoglobin concentration (THC), (b) tissue blood oxygenation (StO_2), (c) scattering (μ'_s), (d) overall attenuation μ_{eff} , (e) optical index.

Table I

Results from co-registered DOT/BPET images. Regions of interest (ROIs) are selected based on BPET images. Tumor to background ratios (TBRs) are calculated by dividing the average value in the ROI by the average value for the entire breast.

	Subject	Average (Breast)	Average (ROI)	TBR
THC (μM)	A	20.3	23.7	1.2
	B	18.7	26.0	1.4
	C	21.3	23.0	1.1
StO_2 (%)	A	92.2	93.0	1.0
	B	87.5	91.3	1.0
	C	73.7	72.0	1.0
μ'_s (cm^{-1})	A	7.9	10.5	1.3
	B	17.6	23.8	1.4
	C	8.9	11.0	1.2
μ_{eff} (cm^{-1})	A	0.99	1.23	1.2
	B	1.41	1.92	1.3
	C	1.10	1.29	1.2
Optical index	A	1.03	1.47	1.5
	B	1.09	1.89	1.7
	C	1.04	1.51	1.5

Table II

Visibility of lesions to DOT and whole-body PET compared with histopathology after imaging. The following abbreviations are used. IDC: invasive ductal carcinoma. DCIS: ductal carcinoma *in situ*. mBR grade: (modified) Bloom-Richardson grade.

Subject	Age	Days between DOT and PET examination	Visible in PET	Visible in DOT	Histopathology (type, mBR grade, size)
1	48	4	Yes	Yes	IDC & DCIS, 3+3+3=9, 2 cm
2	45	0	Yes	Yes	IDC & DCIS, 3+3+3=9, 0.5 cm
3	39	0	Yes	Yes	IDC & DCIS, 2+2+2=6, 3, 4, & 0.8 cm
4	44	0	Yes	Yes	IDC & DCIS, 3+3+1=7, 2, 3 cm
5	44	0	Yes	Yes	IDC & DCIS, 3+2+2=7, 1.8 cm
6	51	0	Yes	No	none (superficial cyst)
7	64	0	Yes	Yes	DCIS, 0.9 cm
8	43	0	Yes	No	none (MRI & US negative results)
9	53	0	No	No	cyst
10	59	0	Yes	Yes	normal tissue (surgical inflammation)
11	44	0	Yes	Yes	IDC & DCIS, 3+3+3=9, 1.5 cm
12	50	13	No	No	mature adipose tissue (possible lipoma)
13	61	0	Yes	No	IDC & DCIS, 1+2+1=4, 0.8 cm
14	37	0	Yes	Yes	IDC & DCIS, 3+3+3=9, 2, 3 cm